Intensity of singular stress fields (ISSFs) in micro-bond test in comparison with ISSFs in pull-out test

doi: https://doi.org/10.1016/j.ijmecsci.2020.105817

Intensity of Singular Stress Fields (ISSFs) in Micro-bond Test in Comparison with ISSFs in Pull-out Test

Dong CHEN [1], Nao-Aki NODA [1,*], Rei Takaki [1], Yoshikazu SANO [1]

[1] Department of Mechanical Engineering, Kyushu Institute of Technology Sensui-Cho 1-1 Tobata-Ku, Kitakyushu-Shi, Fukuoka, Japan

[*] Corresponding author. Email address: noda.naoaki844@mail.kyutech.jp

Abstract. There are several micromechanics tests available for studying the fiber/matrix bonding behaviour. The best-knowns are fragmentation, pull-out test and micro-bond test. This study focuses on the effect of major geometries in micro-bond testing on the intensity of singular stress fields (ISSFs) appearing at the fiber entry/exit points. Then, the ISSFs in micro-bond test are compared with the ISSFs in pull-out test under the same fiber geometry. It is found that the ISSF at the fiber entry point is almost constant independent of the knife gap larger than 10μm. The effect of the bond-length on the ISSF at the fiber entry point is also clarified.

Key words: Micro-bond test, Fiber Pull-out, Fiber/Matrix interface, Finite element method (FEM), Intensity of singular stress field (ISSF).

Nomenclature

FEM	Finite element method
ISSF	Intensity of singular stress field
Point A	Fiber far intersection
Point E	Fiber near intersection
E, E_F, E_M	Young's modulus
ν, ν_F, ν_M	Young's modulus
G, G_F, G_M	Shear modulus
K, K_σ, K_τ	Intensity of singular stress field (ISSF)
σ_x	Tension or compression stress
l_b	Fiber bonded length
l_g	Knife gap openning
D	Width of the fiber
P	Pull-force on the free end of fiber
α, β	Dundurs' material composite parameters
λ, λ_1, λ_2	Singular index
e_{min}	Minimum element size in FEM
r_A, r_E, r_{A^*}, r_{E^*}	Distance from Point A or Point E along the interface
Subscripts	
F	Fiber
M	Matrix
FEM	Corresponding values in FEM analysis
A	Corresponding values at Point A
E	Corresponding values at Point E
*	Corresponding values in reference model

1. Introduction

Wide application of fiber reinforced composites technology in various fields is based on taking advantage of the high strength and high stiffness of fibers. There are several micromechanics tests available to study the fiber/matrix bonding behavior. Pull-out test and micro-bond test are very popular at present. For example, Scheer *et al* [1] experimentally investigated interfacial peeling of reinforcing fibers in micro-bond test focusing on the energy release rate. Zhandarov *et al* [2,3] investigated the pull-out force

versus displacement in pull-out test and micro-bond test. Hann *et al* [4] investigated the effect of contact angle, loading position, and loading type in micro-bond test, by using the finite element method (FEM). Ash *et al* [5] investigated the effect of bead geometry and knife angle in micro-bond test. Those studies showed that the macroscopic properties of the composite can be improved by increasing the fiber/matrix debonding strength [6,7]. However, the macroscopic properties are rarely proportional to the microscopic properties. Moreover, the debonding strength varies depending on the testing method and testing conditions.

Fig. 1(a) shows a single fiber pull out and Fig. 1(b) shows a micro-bond test commonly used. It should be noted that even under the same fiber/matrix combination the experiment results of pull-out strength in Fig. 1(a) is different from that in micro-bond test in Fig. 1(b). Although those tests provide valuable information, the results are strongly depending on the specimen geometry, fiber aspect ratio and other experiment conditions. In Fig. 1(a) and (b), intensities of singular stress fields (ISSFs) control the fiber/matrix interface debonding. In other words, to clarify the fiber/matrix interface information, it is necessary to evaluate the intensity of singular stress fields (ISSFs) at the fiber entry/exit points. In this paper, therefore, the ISSFs will be compared between the pull-out and the micro-bond test to clarify the difference under the same material combination. The effects of geometrical factors on the ISSFs will be also clarified to establish suitable testing conditions. The final goal of this study is to clarify the fiber pull out mechanism toward designing suitable fiber reinforced composites.

2. Modelling and intensity of singular stress filed (ISSF)

2.1 Modelling of micro-bond test and fiber pull-out test

Fig. 1(a) shows a single fiber partially embedded in a semi-infinite resin matrix region. In the previous paper [8,9], by applying the finite element method (FEM), a two-dimensional rectangular shaped fiber subjected to pull-out force was considered as well as a rectangular shaped large region of the matrix. Then, the ISSF was discussed at the fiber end Point A* and the fiber/surface entry Point E*. And the results were compared with the ISSFs of a rectangular inclusion problem [10]. In Fig. 1(a) the green part represents the fiber and the grey portion represents matrix. The preliminarily FEM analysis shows that the rectangular dimension of the matrix should be set to be 4000 times of the width of the fiber to express the semi-infinite plate. Under this condition, the ISSF is independent of the dimension of the matrix.

Fig. 1(b) illustrates a micro-bond test in contrast to the fiber pull-out in Fig. 1(a). In this modelling, a two-dimensional rectangular shaped fiber is also considered similar to Fig. 1(a) under the tensile force P. Instead of a semi-infinite resin region, a rectangular shaped resin of droplet is considered as shown in Fig. 1(b). Here, the dark portion means constraints. In reality, the resin matrix in micro-bond test has an irregular sphere shape and the knife is used to restrain the resin matrix. Although the contact angle in micro-bond test is usually $\theta_c = \frac{\pi}{6} \sim \frac{\pi}{4}$ [2] in Fig. 1(b), the contact angle $\theta_c = \frac{\pi}{2}$ is assumed in Fig. 1(b) to compare with the ISSFs under the pull-out test in Fig. 1(a). Under this assumption, the singular indexes at Point E and Point E* are equal. In both

models in Fig. 1(a) and (b), perfectly bonded interface is assumed between the resin and the fiber with zero interface thickness. Therefore, the material properties around the interface vary in a stepwise manner. Notations E_F, ν_F, E_M, ν_M represent the Young's modulus and Poisson's ratio of fiber and matrix respectively. Notation D denotes the diameter of the fiber, which is the width of the fiber in the present 2D modelling. A uniform tensile stress is distributed at the end of the fiber, and the total force is P. In other words, $P/D = 1[N \cdot mm^{-1}]$ is normalized to analysis the ISSF.

< Insert **Fig. 1.** Here>

In fiber pull-out test in Fig. 1(a), Point A* denotes the fiber end, and Point E* denotes the fiber/surface entry point. Notation l_b denotes the axial bonded length from the end Point A* to the entry Point E* before applying load P.

In micro-bond test in Fig. 1(b), Point E denotes the fiber entry point closer to the load and constraints and Point A denotes the fiber exit point. Notation l_b denotes the axial length of the bonded area from Point A to Point E before applying load P. In this modelling, the rectangular shaped droplet is assumed as shown in Fig. 1(b) with the large width of the droplet in the x-direction as $l_b/2$ on each side. In other words, in this study, the 2D square shape of the droplet is assumed. Notation l_g denotes the horizontal distance from the tip of the constraint knife to the surface of the fiber assuming the symmetry on both sides in Fig. 1(b). Usually, the bonded area l_b is chosen to be less than $250\mu m$ in micro-bond experiment [1,2,4–7,11].

In this study, the ISSF in Fig. 1 is mainly discussed by varying l_b and l_g under plane strain. In the Cartesian x- and y-coordinates shown in Fig. 1, the y-direction corresponds to the axial direction of the fiber, and the x-direction corresponds to the radial direction of the fiber. Notation r_i, $(i = \mathrm{A}, \mathrm{E}, \mathrm{E}^*)$, denotes the distance from Point i, $(i = \mathrm{A}, \mathrm{E}, \mathrm{E}^*)$ in the y direction and $r_i = 0$ means Point i. It should be noted that shear-lag theory is widely used for considering shear stress distributions along fiber interface [12–14]. However, this theory is simply based on one dimensional assumption of the fiber and cannot express the ISSF. For example, although theory results in the critical force proportional to the bonded length, the real ISSF at the entry point is not proportional to the bonded length [8,9].

2.2 Singular stress field at the fiber entry/exit points

The normal singular stress, which may cause debonding at the entry point, can be expressed as follows: [15]

$$\sigma_x^i = \frac{K_{\sigma,\lambda_1}^i}{r_i^{1-\lambda_1}} + \frac{K_{\sigma,\lambda_2}^i}{r_i^{1-\lambda_2}}, (i = \mathrm{A}, \mathrm{E}, \mathrm{E}^*) \tag{1}$$

Here λ_1 and λ_2 are singular indexes, which can be calculated by solving the following characteristic equations [16,17].

$$
\begin{aligned}
&4sin^2(\pi\lambda)\left\{sin^2\left(\frac{\pi\lambda}{2}\right)-\lambda^2\right\}\beta^2+4\lambda^2sin^2(\pi\lambda)\alpha\beta\\
&+\left\{sin^2\left(\frac{\pi\lambda}{2}\right)-\lambda^2\right\}\alpha^2+4\lambda^2sin^2(\pi\lambda)\beta\\
&+2\left\{\lambda^2\cos(2\pi\lambda)+sin^2\left(\frac{\pi\lambda}{2}\right)\cos(\pi\lambda)+\frac{1}{2}sin^2(\pi\lambda)\right\}\alpha\\
&+sin^2\left(\frac{3\pi\lambda}{2}\right)-\lambda^2=0
\end{aligned}
\tag{2}
$$

Here, α, β denote bimaterial parameters of Dundurs [18], and G_F and G_M are shear modulus, which can be transformed from Young's modulus E_F, E_M and Poisson's Ratios ν_F, ν_M. Subscripts M, F represent the matrix and the reinforcing fiber, respectively. In this study, analysis is carried out under plane strain.

$$
\left.
\begin{aligned}
\alpha&=\frac{G_F(\kappa_M+1)-G_M(\kappa_F+1)}{G_F(\kappa_M+1)+G_M(\kappa_F+1)},\quad \beta=\frac{G_F(\kappa_M-1)-G_M(\kappa_F-1)}{G_F(\kappa_M+1)+G_M(\kappa_F+1)},\\
\kappa_i&=\begin{cases}(3-\nu_i)/(1+\nu_i) & (Plain\ stress)\\ (3-4\nu_i) & (Plain\ strain)\end{cases}(i=M,F)
\end{aligned}
\right\}
\tag{3}
$$

For the material combination as shown in Table 1, $\alpha=0.9071$, $\beta=0.2016$, $\lambda_1=0.6592$, $\lambda_2=0.9992$. Here, λ_2 is close to 1, which means that equation (1) can be written as equation (4).

$$
\sigma_x^i=\frac{K_{\sigma,\lambda_1}^i}{r_i^{1-\lambda_1}}+\frac{K_{\sigma,\lambda_2}^i}{r_i^{1-\lambda_2}}\cong\frac{K_{\sigma,\lambda_1}^i}{r_i^{1-\lambda_1}},\ (i=\mathrm{A},\mathrm{E},\mathrm{E}^*)
\tag{4}
$$

$$K_\sigma^i \cong K_{\sigma,\lambda_1}^i = \lim_{r\to 0}\left[\sigma_x^i(r_i)\cdot r_i^{1-\lambda_1}\right],\ (i = \mathrm{A},\mathrm{E},\mathrm{E}^*)$$

(5)

2.3 Proportional method by using FEM

Finite element method (FEM) analysis should be well conducted and may require experience and skills for engineering applications [19–27]. In this analysis, a mesh independent proportional method is used to calculate the ISSF K_σ^i defined in equation (5). Since λ_2 is close to 1, the second term can be omitted, the ISSF can be calculated from the ratio of FEM stress $\sigma_{x,i}^{FEM}(r_i)$ as shown in equation (6) [15–17,28].

$$\frac{K_{\sigma,\lambda_1,i}}{K_{\sigma,\lambda_1,j}} = \frac{\sigma_{x,i}^{FEM}(r_i)}{\sigma_{x,j}^{FEM}(r_j)},\ (i,j = \mathrm{A},\mathrm{E},\mathrm{E}^*)$$

(6)

As shown in Table 2, the stress distributions $\sigma_{x,FEM}^E(r_E)$ and $\sigma_{x,FEM}^A(r_A)$ varies depending on the FEM mesh size. However, the FEM stress ratio $\sigma_{x,FEM}^E(r_E)/\sigma_{x,FEM}^A(r_A)$ is almost the same independent of mesh size. This is because the same mesh pattern is applied to the singular stress region to cancel the FEM error. The FEM stress ratio in Table 2 can be regarded as the real stress ratio although the FEM stress cannot express the real singular stress. Since the stress ratio can be obtained accurately in Table 2, the ISSF of the pull-out problem can be obtained from the ISSF of reference problems with the ratio as shown in equation (6).

3. Results and Discussion

3.1 Bond length l_b effect on ISSF in micro-bond test

To investigate the bond length effect l_b on the ISSFs, other dimensions are fixed as knife gap $l_g = 20\mu\text{m}$, fiber diameter $D = 20\mu m$ and contact angle $\theta_C = \frac{\pi}{2}$ with the material combinations in Table 1. The ISSFs can be calculated by the proportional method. Here, the reference values are given as the results of pull-out in the previous study [8,9].

As shown in Fig. 2 and Table 3, the ISSFs at Points A, E, and E* decrease with increasing l_b. In micro-bond test, tensile normal stress appears near the entry Point E and compressive normal stress appears near the exit Point A. Those stresses are similar to the stresses in pull-out test where tensile normal stress appears near the entry point E*and compressive normal stress appears near the end Point A*. Therefore, the ISSF at Point E is under tension but the ISSF at Point A is under compression. From those results, no matter how the l_b changes, Point E in micro-bond test is the most critical for debonding. The ISSFs at Point E and Point E* decrease in a similar way by increasing l_b. Table 3 and Fig. 3 shows ISSF ratios $\frac{-K_\sigma^A}{K_\sigma^E}$ and $\frac{K_\sigma^{E^*}}{K_\sigma^E}$. As shown in Table 3 and Fig. 3, the ratio $\frac{-K_\sigma^A}{K_\sigma^E}$ decreases significantly with increasing l_b. Instead, the ratio $\frac{K_\sigma^{E^*}}{K_\sigma^E}$ is almost constant as $\frac{K_\sigma^{E^*}}{K_\sigma^E} \cong 0.75$. In other words, the ISSF at Point E in micro-bond test is about 1.5 times larger than that of Point B* in pull-out test.

< Insert **Fig. 2.** Here>

< Insert **Fig. 3.** Here>

3.2 Knife gap l_g effect on ISSF in micro-bond test

Table 4 and Fig. 4 illustrate the effect of the knife gap l_g on the ISSF K_σ^E at the entry Point E. Here, the droplet dimensions $l_b = 100\mu m, 200\mu m, 400\mu m$ are assumed. This is because in the previous experiment [1,2,4–7,11], the bonded length l_b, which is nearly equal to the droplet dimension, is in the range $50\mu m$~$400\mu m$ in most cases. The ISSF values for $l_g \leq 40$μm varies less than 1% even though the width of the droplet is changed from l_b to $2l_b$. Therefore, to calculate the ISSF at Point E when $l_g = 80\mu m$ and $l_b = 100$μm, the width of the droplet in FEM is adjusted to $2l_b$ instead of l_b. As shown in Table 4 and Fig. 4, the ISSF K_σ^E increases significantly with decreasing l_g, when $l_g < 10\mu m$. However, when l_g becomes larger than a certain value, that is, $l_g \geq D$ =$20\mu m$, l_g has less influence on K_σ^E. Care should be taken for the ISSF in Fig.1 (b) for small knife gap $l_g < 10\mu m$ because the ISSF varies very sensitively for small change of l_g as shown in Fig.4. Instead, $l_g > D = 20\mu m$ can be recommended for micro-bond testing since the ISSF K_σ^E becomes almost constant. For small $l_b = 100\mu m$, however, the ISSF increases slightly with increasing $l_g \geq D = 20\mu m$. This is because of the bend deformation of the droplet.

< Insert **Fig. 4.** Here>

Fig. 5 illustrates the matrix surface deformation $u_y^E(x)$ due to the fiber pull out force $\mathrm{P} = 1\mathrm{MPa} \times 0.02\mathrm{mm} \times 1\mathrm{mm} = 0.02\mathrm{N}$ around the fiber entry Point E when $l_b = 400\mu\mathrm{m}$ and $l_b = 100\mu\mathrm{m}$. The x-axis shows the distance from Point E at $x = 0$ to the knife edge at $x = l_g$ where the deformation is constrained. Deformation when $l_b = 400\mu\mathrm{m}$ is relatively smaller than that when $l_b = 100\mu\mathrm{m}$. Table 5 shows the displacement at Point E $u_y^E(0)$, the displacement at the exit Point A $u_y^A(0)$, the fiber elongation $u_y^E(0) - u_y^A(0)$, and the angle change at Point E $\Delta\theta_C$. As shown in Fig. 6, $u_y^E(0)$ at Point E and $u_y^A(0)$ at Point A increase almost linearly with increasing l_g. Instead, the ISSF K_σ^E does not control $u_y^E(0)$ or $u_y^A(0)$. As shown in Table 5 and Fig. 7, the ratio $K_\sigma^E/\Delta\theta_C$ between the ISSF K_σ^E and the surface angle change $\Delta\theta_C$ is almost constant. In other words, $\Delta\theta_C$ mainly controls K_σ^E.

The ISSF increases significantly for small value of l_g as shown in Fig. 4. This is because the surface angle change $\Delta\theta_C$ is large due to the smaller l_g compared to $u_y^E(0)$. Care should be taken for the small knife gap $l_g < 10\mu m$ in micro-bond test because of the ISSF controlling the experiment varies very sensitively by the slight change of l_g in Fig. 4. Some previous studies [29–31] suggested that the gap should be as small as possible. However, in the sense of similarity between micro-bond test and pull-out test, a certain gap should be kept.

< Insert **Fig. 5.** Here>

< Insert **Fig. 6.** Here>

< Insert **Fig. 7.** Here>

4. Conclusions

To clarify the fiber pull out mechanism toward designing suitable fiber reinforced composites, this study focused on the micro-bond test commonly used for investigating fiber/matrix bonding behaviour. The intensity of singular stress field (ISSF) was analysed at the fiber entry/exit points by using a mesh-independent proportional method. The ISSFs in micro-bond test were compared with the ISSFs in pull-out test. The conclusions can be summarized in the following way.

1. In micro-bond test in Fig.1(b), the ISSF at the entry Point E is under tension but the ISSF at the exit Point A is under compression. No matter how the bond length l_b changes, Point E in Fig.1(b) is the most dangerous point. Instead, in pull-out test in Fig.1(a), Point A* can be more dangerous compared with Point E* when l_b is shorter.

2. The ISSFs in micro-bond test in Fig.1(b) at the fiber entry/exit points in micro-bond test decrease with increasing the bond length l_b. Similarly, the ISSFs in pull-out test in Fig.1(a) at the fiber entry/end points decrease with increasing the bond length l_b. The ISSF at the entry Point E in micro-bond test is about 1.5 times of that of pull-out test at Point E*when l_b is the same as shown in Fig. 3.

3. Care should be taken for the small knife gap $l_g < 10\mu m$ because the ISSF at Point E is very sensitive for slight change of l_g in Fig.4. Instead, $l_g > D = 20\mu m$ can be recommended since the ISSF K_σ^E becomes almost constant. For small $l_b = 100\mu m$,

however, the ISSF increases slightly with increasing $l_g > D = 20\mu m$. This is because of the bend deformation of the droplet.

4. With increasing knife gap l_g, the displacement $u_y^E(0)$ at Point E and the displacement $u_y^A(0)$ at Point A increase almost linearly as shown in Fig. 6. The ratio of the ISSF K_σ^E to the surface angle change $\Delta\theta_C = 90° - \theta_C$ is almost constant as shown in Fig. 7. In other words, $\Delta\theta_C$ mainly controls K_σ^E.

Reference

[1] Scheer RJ, Nairn JA. A Comparison of Several Fracture Mechanics Methods for Measuring Interfacial Toughness with Microbond Tests. J Adhes 1995;53:45–68. doi:10.1080/00218469508014371.

[2] Pisanova E, Zhandarov S, Mäder E, Ahmad I, Young RJ. Three techniques of interfacial bond strength estimation from direct observation of crack initiation and propagation in polymer-fibre systems. Compos Part A Appl Sci Manuf 2001;32:435–43. doi:10.1016/S1359-835X(00)00054-3.

[3] Zhandarov S, Mäder E. Characterization of fiber/matrix interface strength: Applicability of different tests, approaches and parameters. Compos Sci Technol 2005;65:149–60. doi:10.1016/j.compscitech.2004.07.003.

[4] Hann LP, Hirt DE. Simulating the microbond technique with macrodroplets. Compos Sci Technol 1995;54:423–30. doi:10.1016/0266-3538(95)00080-1.

[5] Ash JT, Cross WM, Svalstad D, Kellar JJ, Kjerengtroen L. Finite element evaluation of the microbond test: meniscus effect, interphase region, and vise angle. Compos Sci Technol 2003;63:641–51. doi:10.1016/S0266-3538(02)00256-7.

[6] Baley C, Grohens Y, Busnel F, Davies P. Application of Interlaminar Tests to Marine Composites. Relation between Glass Fibre/Polymer Interfaces and Interlaminar Properties of Marine Composites. Appl Compos Mater 2004;11:77–98. doi:10.1023/B:ACMA.0000012884.02847.65.

[7] Miller B, Muri P, Rebenfeld L. A microbond method for determination of the shear strength of a fiber/resin interface. Compos Sci Technol 1987;28:17–32. doi:10.1016/0266-3538(87)90059-5.

[8] Noda N-A, Chen D, Takaki R, Inoue A, Zhang G, Sano Y. Intensity of singular stress fields of an embedded fiber under pull-out force . Zair Soc Mater Sci Japan 2018;67:1073–9. doi:10.2472/jsms.67.1073.

[9] Noda N, Chen D, Zhang G, Sano Y. Single-fiber pull-out analysis comparing the intensities of singular stress fields (ISSFs) at fiber end / entry points. Int J Mech Sci 2020;165:105196. doi:10.1016/j.ijmecsci.2019.105196.

[10] Noda N-A, Wang Q, Uemura Y, Kawashima Y. Singular integral equation method in the analysis of interaction between rectangular inclusions. JSME Int Journal, Ser A Mech Mater Eng 1998;41:303–8.

[11] Gao S-L, Mäder E, Zhandarov SF. Carbon fibers and composites with epoxy resins: topography, fractography and interphases. Carbon N Y 2004;42:515–29. doi:10.1016/j.carbon.2003.12.085.

[12] Goda K. Semi-discretization analysis for the shear-lag model with a viscoelastic

matrix and its application to creep-rupture simulation using the bis method. Nihon Kikai Gakkai Ronbunshu, A Hen/Trans Japan Soc Mech Eng Part A 2000;66:480–8. doi:10.1299/kikaia.66.480.

[13] Hedgepeth JM, Van Dyke P. Local Stress Concentrations in Imperfect Filamentary Composite Materials. J Compos Mater 1967;1:294–309. doi:10.1177/002199836700100305.

[14] Batdorf SB. Note on shear interaction between two fibers. Eng Fract Mech 1983;18:1207–10. doi:10.1016/0013-7944(83)90014-0.

[15] Miyazaki T, Noda N-A, Sano Y. A precise and efficient analytical method to obtain two distinct intensities of singular stress fields for single lap joint. J Japan Inst Electron Packag 2018;21:166–77. doi:10.5104/jiep.21.166.

[16] Bogy DB. Edge-bonded dissimilar orthogonal elastic wedges under normal and shear loading. J Appl Mech Trans ASME 1964;35:460–6. doi:10.1115/1.3601236.

[17] Bogy DB. Two edge-bonded elastic wedges of different materials and wedge angles under surface tractions. J Appl Mech Trans ASME 1971;38:377–86. doi:10.1115/1.3408786.

[18] Dundurs J. Effect of Elastic Constants on Stress in a Composite Under Plane Deformation. J Compos Mater 1967;1:310–22. doi:10.1177/002199836700100306.

[19] Noda N-A, Chen X, Sano Y, Wahab MA, Maruyama H, Fujisawa R, et al. Effect of pitch difference between the bolt-nut connections upon the anti-loosening performance and fatigue life. Mater Des 2016;96:476–89. doi:10.1016/j.matdes.2016.01.128.

[20] Noda N-A, Takaki R, Shen Y, Inoue A, Sano Y, Akagi D, et al. Strain rate concentration factor for flat notched specimen to predict impact strength for polymeric materials. Mech Mater 2019;131:141–57. doi:10.1016/j.mechmat.2019.01.011.

[21] Wang Z, Noda N-A, Ueno M, Sano Y. Optimum Design of Ceramic Spray Coating Evaluated in Terms of Intensity of Singular Stress Field. Steel Res Int 2017;88. doi:10.1002/srin.201600353.

[22] Stern M, Soni ML. On the computation of stress intensities at fixed-free corners. Int J Solids Struct 1976;12:331–7. doi:10.1016/0020-7683(76)90023-8.

[23] Atkinson C, Avila J, Betz E, Smelser RE. The rod pull out problem, theory and experiment. J Mech Phys Solids 1982;30:97–120. doi:10.1016/0022-5096(82)90019-9.

[24] Povirk GL, Needleman A. Finite element simulations of fiber pull-out. J Eng Mater Technol Trans ASME 1993;115:286–91. doi:10.1115/1.2904220.

[25] Freund LB. Axial force needed to slide a circular fiber along a hole in an elastic

material and implications for fiber pull-out. Eur J Mech A/Solids 1992;11:1–19.

[26] Zhang X, Liu H-Y, Mai Y-W. Effects of fibre debonding and sliding on the fracture behaviour of fibre-reinforced composites. Compos Part A Appl Sci Manuf 2004;35:1313–23. doi:10.1016/j.compositesa.2004.03.011.

[27] Hutchinson JW, Jensen HM. Models of fiber debonding and pullout in brittle composites with friction. Mech Mater 1990;9:139–63. doi:10.1016/0167-6636(90)90037-G.

[28] Oda K, Kamisugi K, Noda NA. Analysis of stress intensity factor for interface cracks based on proportional method. Nihon Kikai Gakkai Ronbunshu, A Hen/Trans Japan Soc Mech Eng Part A 2009;75:476–82. doi:10.1299/kikaia.75.476.

[29] Chou CT, Gaur U, Miller B. The effect of microvise gap width on microbond pull-out test results. Compos Sci Technol 1994;51:111–6. doi:10.1016/0266-3538(94)90161-9.

[30] Latour RA, Black J, Miller B. Fracture mechanisms of the fiber/matrix interfacial bond in fiber reinforced polymer composites. Surf Interface Anal 1991;17:477–84. doi:10.1002/sia.740170711.

[31] Rao V, Herrera-Franco P, Ozzello AD, Drzal LT. A Direct Comparison of the Fragmentation Test and the Microbond Pull-out Test for Determining the Interfacial Shear Strength. J Adhes 1991;34:65–77. doi:10.1080/00218469108026506.

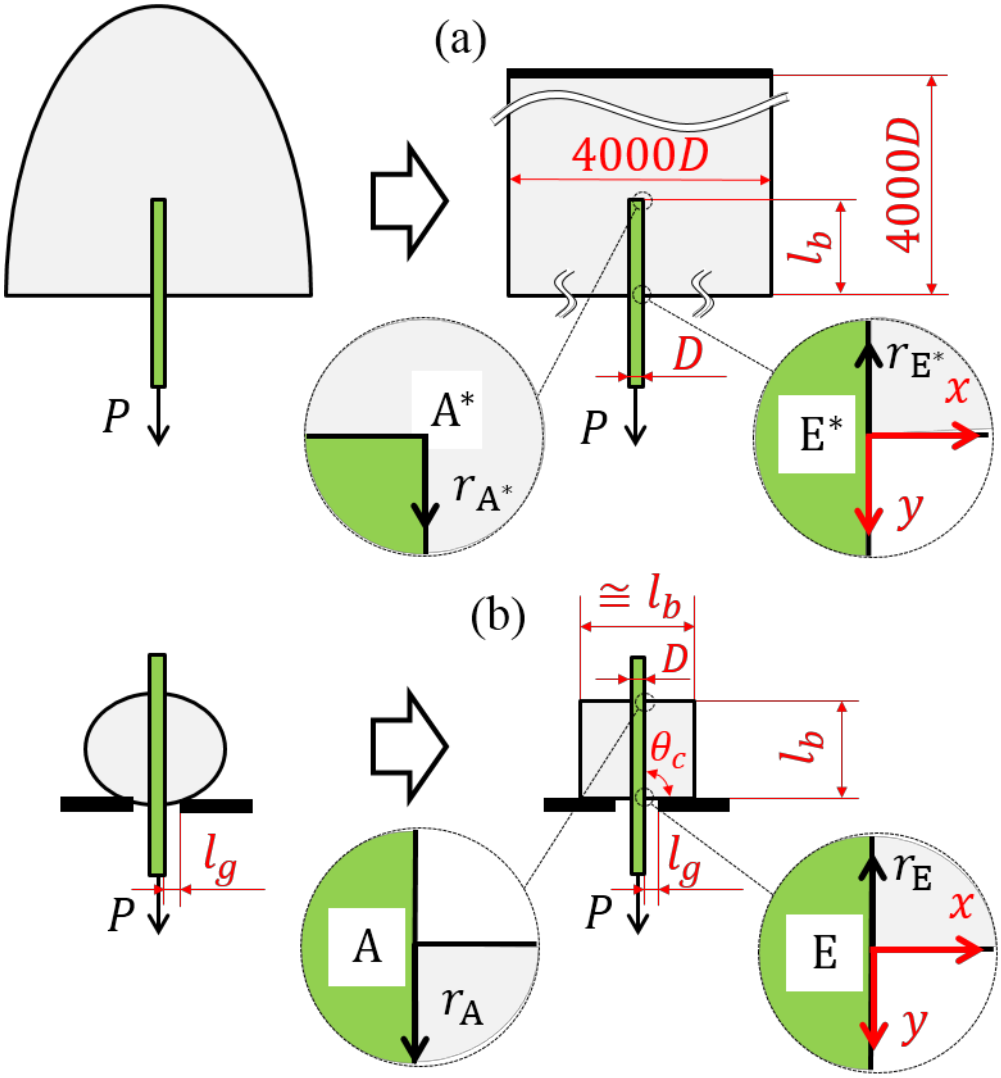

Fig. 1(a). Modelling of pull-out of a fiber. **(b).** Modelling of micro-bond test of a fiber

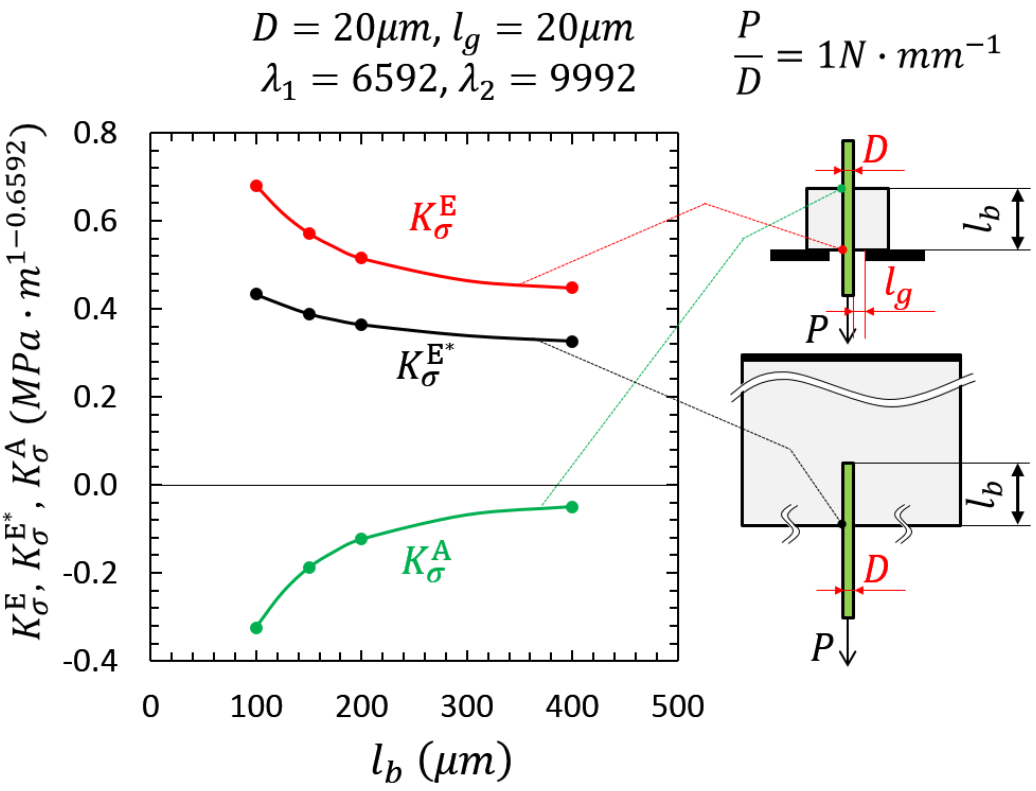

Fig. 2. ISSF variations K_σ^A, K_σ^E , $K_\sigma^{E^*}$ by varying $l_b$when $l_g = 20\mu m$ in micro-bond test

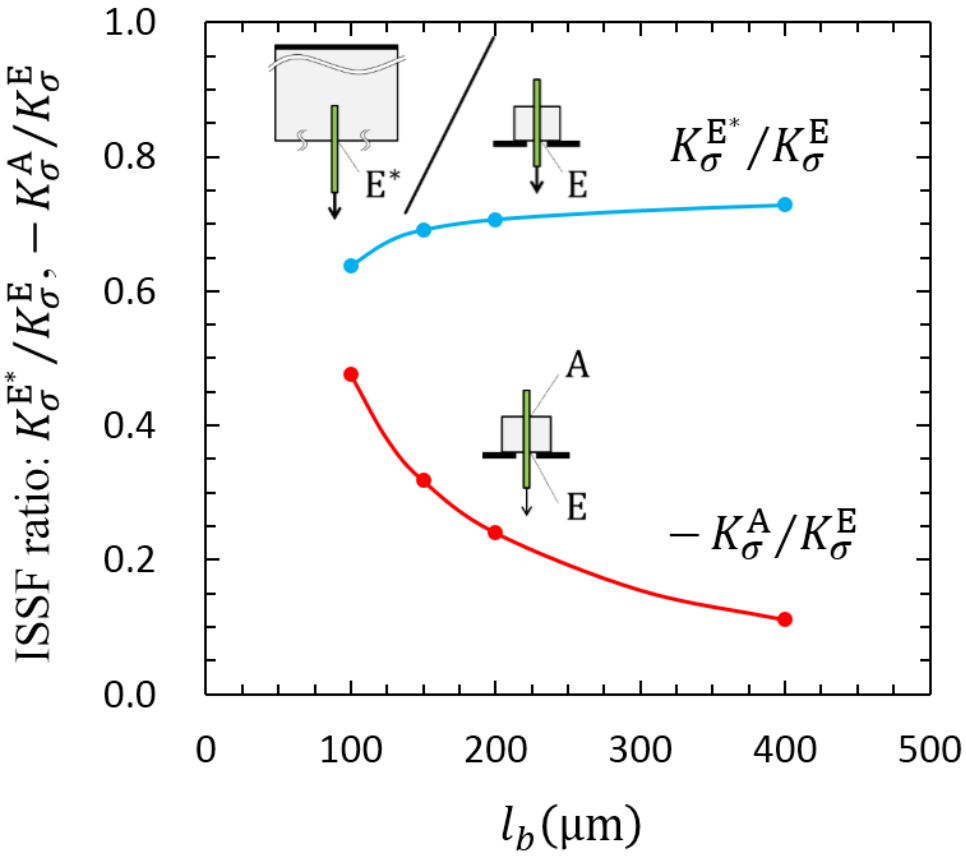

Fig. 3. ISSF ratio variations by varying l_b

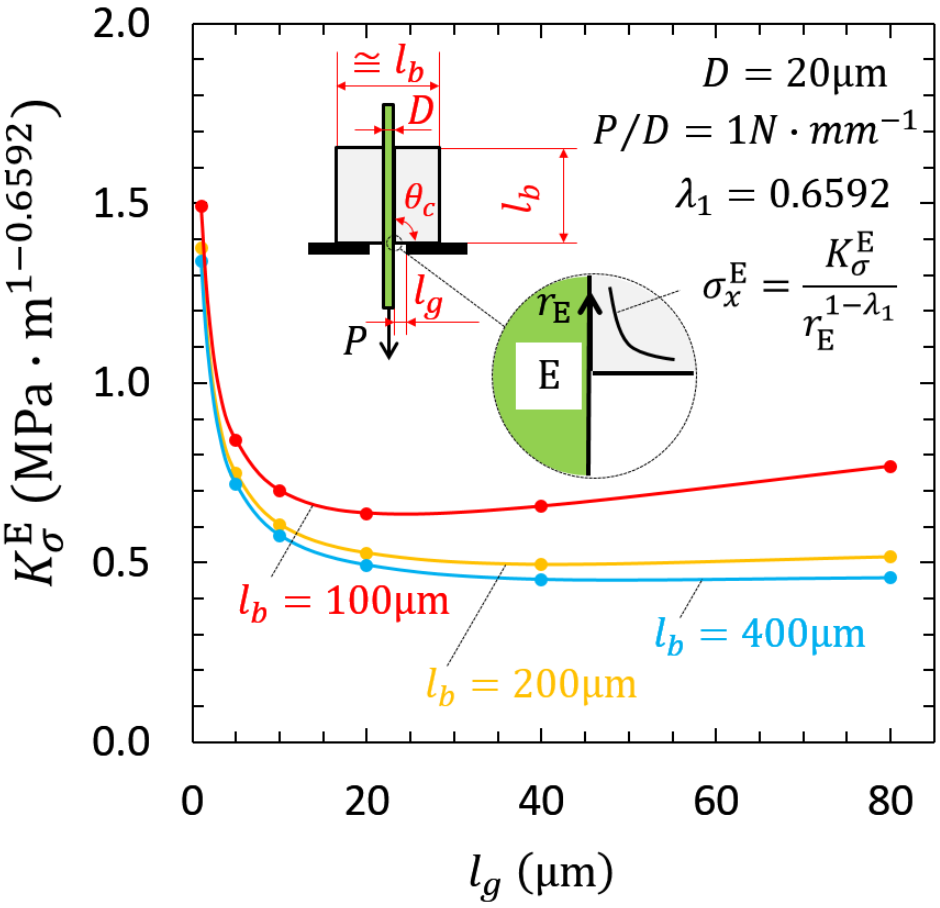

Fig. 4. ISSF variation K_σ^E by varying l_g when $l_b = 100\mu m, 200\mu m, 400\mu m$

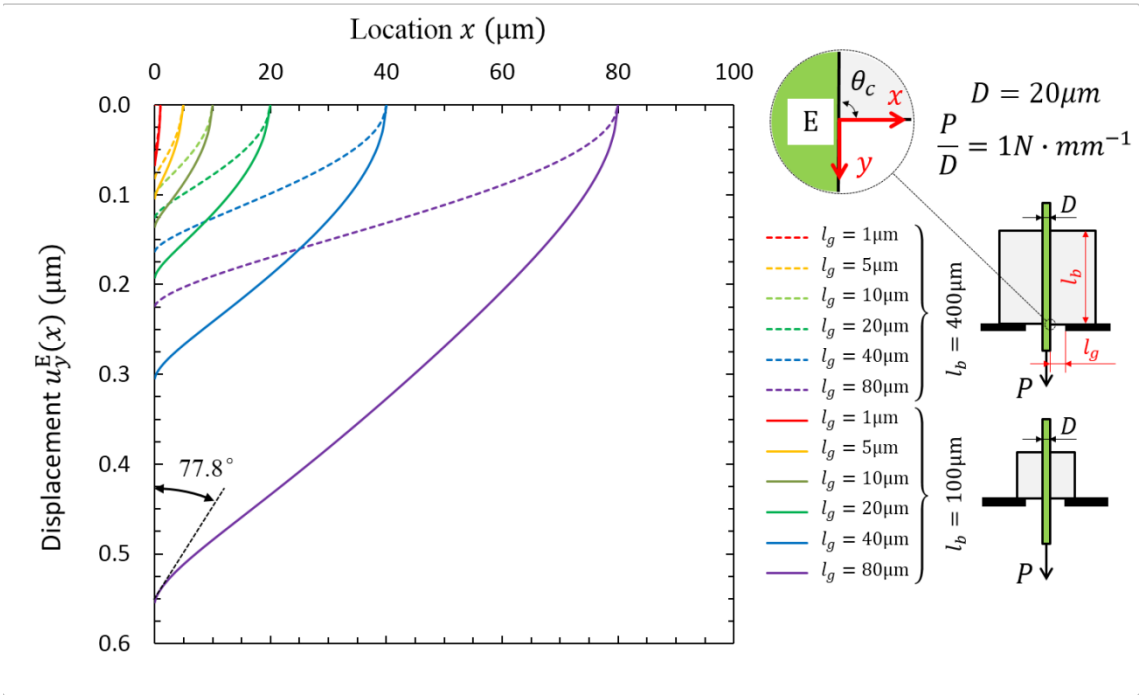

Fig. 5. Fiber deformation at the unrestrained surface

by varying knife gap l_g for fixed $l_b = 100\mu m$ and $l_b = 400\mu m$

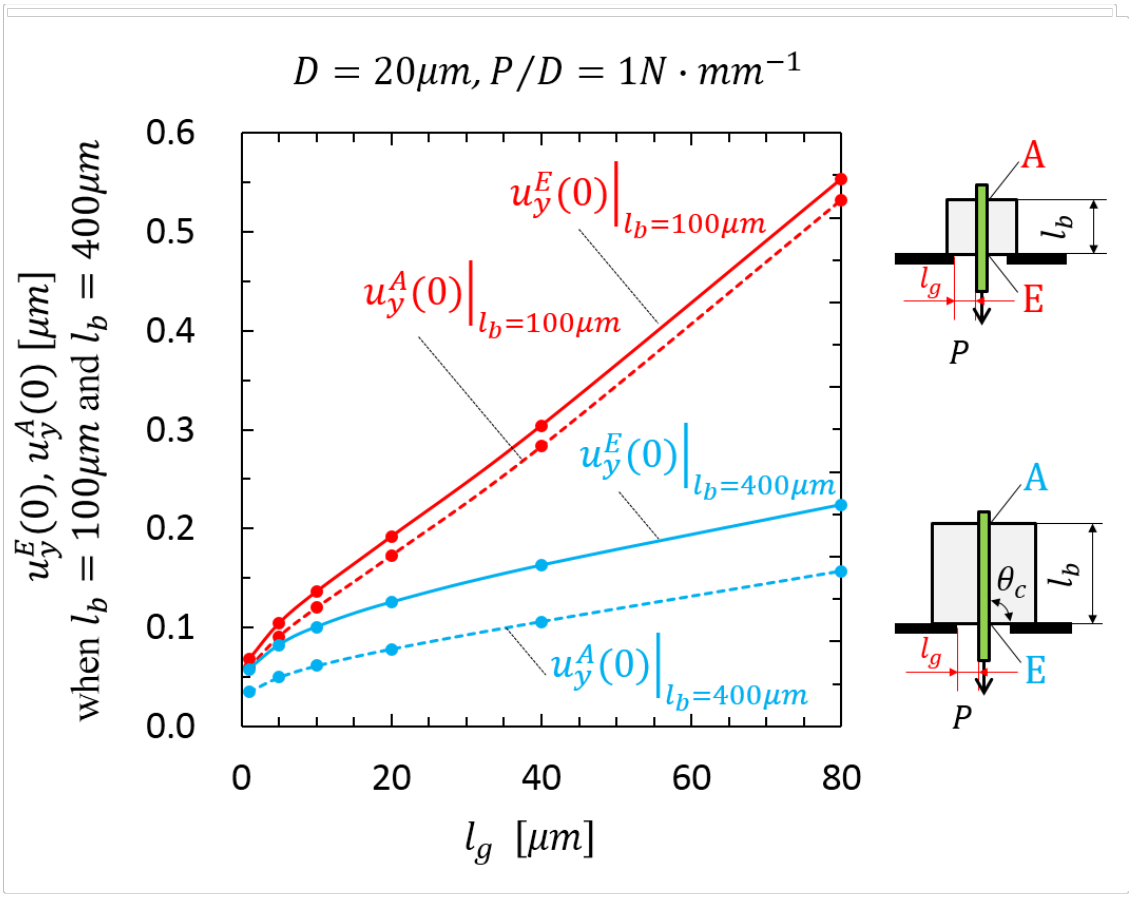

Fig. 6. l_g effect on $u_y^E(0)$ and $u_y^A(0)$, when $l_b = 100\mu m$ and $l_b = 400\mu m$.

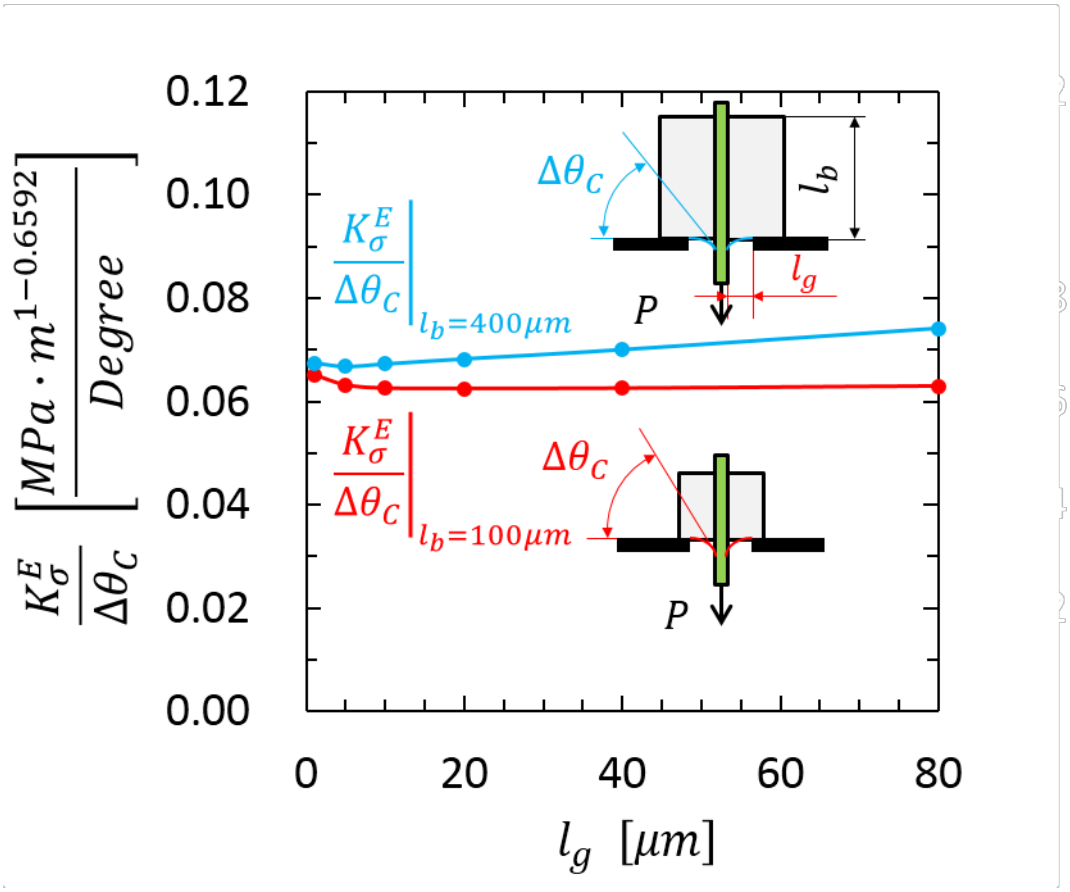

Fig. 7. Ratio of ISSF and contact angle deformation

Table 1. Mechanical properties

	Young's Modulus	Poisson's Ratio	Material
Fiber	75GPa	0.17	Glass fiber
Matrix	3.3GPa	0.35	Epoxy

Table 2. FEM Stress ratio with $\lambda_1^A = 0.6592$ when $l_{in} = 100\mu m$ between Point E and Point A in Fig. 1(b) for the material combination in Table 1.

Smallest mesh size $e_{min} = 3^{-9}$			Smallest mesh size $e_{min} = 3^{-10}$		
$\frac{r}{e_{min}}$	$\sigma_{x,FEM}^E(r_E)$ [MPa]	$\frac{\sigma_{x,FEM}^E(r_E)}{\sigma_{x,FEM}^A(r_A)}$	$\frac{r}{e_{min}}$	$\sigma_{x,FEM}^E(r_E)$ [MPa]	$\frac{\sigma_{x,FEM}^E(r_E)}{\sigma_{x,FEM}^A(r_A)}$
0.0	1.211	-1.376	0.0	1.724	-1.371
0.5	1.033	-1.371	0.5	1.469	-1.368
1.0	0.756	-1.365	1.0	1.075	-1.366
1.5	0.630	-1.359	1.5	0.896	-1.364
2.0	0.594	-1.356	2.0	0.845	-1.363

Table 3. ISSF variations K_σ^A, K_σ^E , $K_\sigma^{E^*}$ by varying $l_b$when $l_g = 20\mu m$ in micro-bond test, ( ): ISSF ratio variations K_σ^A/K_σ^E and $K_\sigma^{E^*}/K_\sigma^E$ by varying l_b

l_b[μm]	K_σ^E $\left(\frac{K_\sigma^E}{K_\sigma^E}\right)$	K_σ^A $\left(\frac{K_\sigma^A}{K_\sigma^E}\right)$	$K_\sigma^{E^*}$ $\left(\frac{K_\sigma^{E^*}}{K_\sigma^E}\right)$
100	0.680 (1.000)	-0.324 (-0.476)	0.433 (0.637)
150	0.562 (1.000)	-0.179 (-0.318)	0.389 (0.691)
200	0.515 (1.000)	-0.124 (-0.240)	0.364 (0.707)
400	0.448 (1.000)	-0.0498 (-0.111)	0.326 (0.728)

Table 4. ISSF variation K_σ^E by varying l_g. ( ): $K_\sigma^E|_{l_b} / K_\sigma^E|_{l_b=100\mu m}$.

l_b [μm] \ l_g [μm]	1	5	10	20	40	80
100	1.492 (1.000)	0.840 (1.000)	0.700 (1.000)	0.637 (1.000)	0.656 (1.000)	0.768 (1.000)
200	1.377 (0.923)	0.749 (0.891)	0.606 (0.866)	0.526 (0.826)	0.494 (0.753)	0.515 (0.671)
400	1.337 (0.896)	0.718 (0.855)	0.576 (0.822)	0.493 (0.773)	0.453 (0.690)	0.457 (0.595)

Table 5a. Fiber deformation when $l_b = 100\mu m$

Knife gap l_g (μm)	1	5	10	20	40	80
K_σ^E	1.492	0.840	0.700	0.637	0.656	0.768
Displacement $u_y^E(0)$ (μm)	0.0675	0.1041	0.1362	0.1919	0.3042	0.5535
Displacement $u_y^A(0)$ (μm)	0.0593	0.0908	0.1201	0.1729	0.2831	0.5323
Fiber elongation $\Delta l_b = u_y^E - u_y^A$	0.0082	0.0133	0.0161	0.0190	0.0211	0.0212
θ_C after deformation	67.1°	76.7°	78.8°	79.8°	79.5°	77.8°
$\Delta\theta_C = 90° - \theta_C$	22.9°	13.3°	11.2°	10.2°	10.5°	12.2°
$u_y^E(0)/K_\sigma^E$	0.0452	0.1240	0.1945	0.3013	0.4636	0.7210
$K_\sigma^E/\Delta\theta_C$	0.0652	0.0632	0.0625	0.0625	0.0625	0.0629

$D = 20\mu m$

$\frac{P}{D} = 1N \cdot mm^{-1}$

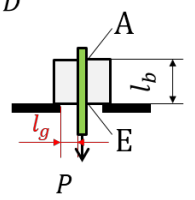

Table 5b. Fiber deformation when $l_b = 400\mu m$

Knife gap l_g (μm)	1	5	10	20	40	80
K_σ^E	1.337	0.718	0.576	0.493	0.452	0.457
Displacement $u_y^E(0)$ (μm)	0.0575	0.0821	0.1004	0.1254	0.1628	0.2241
Displacement $u_y^A(0)$ (μm)	0.0349	0.0495	0.0611	0.0781	0.1058	0.1566
Fiber elongation $\Delta l_b = u_y^E - u_y^A$	0.0226	0.0326	0.0393	0.0473	0.0570	0.0675
θ_C after deformation	70.2°	79.2°	81.4°	82.8°	83.5°	83.8°
$\Delta\theta_C = 90° - \theta_C$	19.8°	10.8°	8.6°	7.2°	6.5°	6.2°
$u_y^E(0)/K_\sigma^E$	0.0430	0.1144	0.1744	0.2545	0.3598	0.4906
$K_\sigma^E/\Delta\theta_C$	0.0674	0.0667	0.0672	0.0682	0.0700	0.0740

$D = 20\mu m$

$\frac{P}{D} = 1N \cdot mm^{-1}$